Article

Microstructure and High Temperature Deformation of Extruded Al-12Si-3Cu-Based Alloy

Seung-Baek Yu and Mok-Soon Kim *

Division of Materials Science and Engineering, Inha University, Incheon 22207, Korea; 22151518@inha.edu
* Correspondence: mskim@inha.ac.kr; Tel.: +82-32-860-7541; Fax: +82-32-862-5546

Abstract: The high temperature deformation behavior of commercial Al-12Si-3Cu-2Ni-1Mg alloy (DM104™) which was fabricated by casting and subsequent hot extrusion was evaluated by compressive tests over the temperature range of 250–470 °C and strain rate range of 0.001–1/s. The extruded alloy had equiaxed grains, spherical Si particles and fine intermetallic phases, such as $\delta(Al_3NiCu)$ and $Q(Al_5Cu_2Mg_3Si_6)$. The true stress-true strain curves from the compressive tests exhibited steady-state flow after reaching the peak stress. A close relationship between the steady-state stress and a constitutive equation for high temperature deformation was observed. Fine equiaxed grains and a dislocation structure within the equiaxed grains were observed in the deformed specimens, suggesting the occurrence of dynamic recrystallization during high temperature deformation.

Keywords: piston alloy; extrusion; compressive test; plastic deformation; high temperature

1. Introduction

Al-Si-based alloys are used widely as a piston materials because of their good specific strength, excellent wear resistance and low coefficient of thermal expansion [1–4]. The addition of Cu and Mg to Al-Si alloys was reported to promote their mechanical properties through the precipitation of the Al_2Cu, Mg_2Si phases [5–8]. Furthermore, it was reported that Ni is a desirable element for improving the mechanical properties of Al-Si-based alloys at elevated temperatures by forming thermally stable Ni-containing intermetallics [9]. To meet the strength requirement of advanced aluminum material for high performance automotive engines, the Al-12Si-3Cu-2Ni-1Mg piston alloy (DM104™) was recently developed by DYP (Dong Yang Piston Co, Ltd., Gyeonggi-do, Korea). The DM104 alloy can be applicable as a forging stock for forged pistons and as a cast piston material. In the case of its use as a forging stock, a careful study of the plastic deformation behavior of the material up to the high temperature region is needed to determine the optimal processing conditions for forging. In this study, the plastic deformation behavior of the extruded Al-12Si-3Cu-2Ni-1Mg alloy was examined using compressive tests over a wide range of temperatures and strain rates. Plastic flow curves were obtained from compressive tests and used to evaluate a constitutive equation. Detailed microstructural observations were made for the specimens before and after deformation.

2. Experimental Section

The material used in this study was a commercial Al-12Si-3Cu-2Ni-1Mg (nominal composition, wt. %) alloy, designated as DM104™, which was fabricated by casting and subsequent hot extrusion. The extrusion billet had a cylindrical shape with a diameter of 90 mm.

Table 1 lists the chemical composition of the as-received alloy (hereafter, "the alloy" or "the billet" denotes DM104 extruded alloy). Cross-sections of the billet were ground using SiC paper up to a grit

number of 2000, and polished using a diamond suspension and colloidal silica. The microstructure was observed using an Olympus PME3-313UN optical microscope (Olympus, Tokyo, Japan) after etching with modified Weak's reagent. The hardness was measured using a Akashi HM-124 Vickers hardness tester (Mitsudoyo, Tokyo, Japan) with a load of 0.1 kg and a dwell time of 10 s. The Vickers hardness was obtained by an average of at least 20 measurements. Cylindrical compression test specimens with a diameter of 5 mm and a height of 7.5 mm were fabricated from the billet. The samples were taken from the 3 cm radius location from the billet edge. Compressive tests were conducted over the temperature range, 250–470 °C and strain rate range 0.001–1/s. The compressive tests were performed up to the true strain of approximately 100% after holding for 15 min at the target temperature. After the compressive test, the sample was quenched in water and cut along the loading axis to observe the microstructure. Phase analysis was conducted by energy dispersive spectroscopy (EDS; Emax 132-10, Horiba, Kyoto, Japan) and X-ray diffraction (XRD; X'pert MPD PRO, Philips, Amsterdam, The Netherlands), and compared with the JMatPro simulation data.

Table 1. Chemical composition of the alloy studied.

Alloy Compositions (wt. %)								
Element	Si	Fe	Cu	Mg	Ni	Ti	V	Zr	Al
DM104	12	0.3	3.2	0.9	2.0	0.1	0.1	0.1	Bal.

3. Results and Discussion

3.1. Microstructure of the As-Received Alloy

Figure 1 shows the etched microstructure of a cross-section. As shown in the figure, the microstructure consisted of well-developed equiaxed grains (see arrow a), spherical Si particles (arrow b) and fine intermetallic phases (arrow c). The mean grain size of the equiaxed grains was measured to be approximately 5 μm. The Vickers hardness value of the matrix was measured to be 90 Hv.
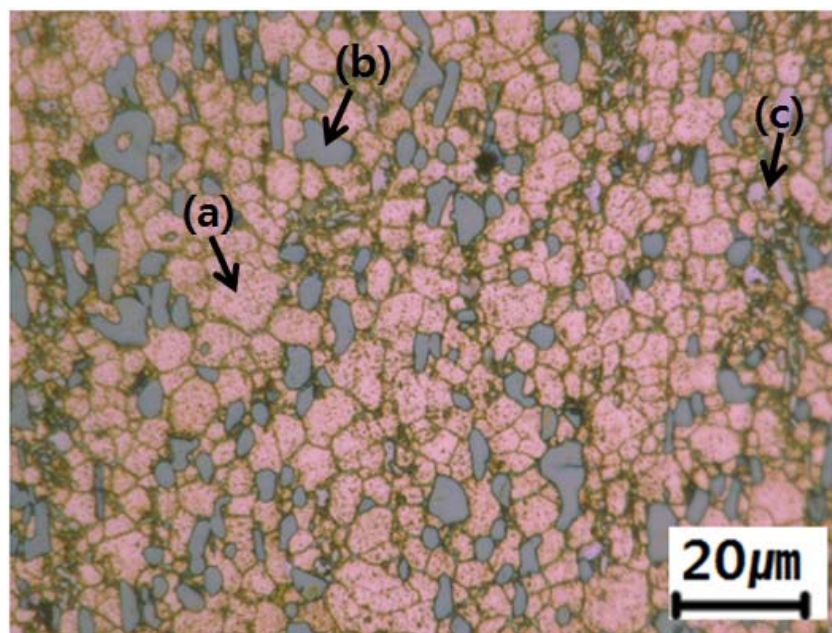

Figure 1. Optical micrograph of the cross-section for as-received alloy.

　　　Figure 2 shows the results of the EBSD analysis data for the cross-section of the alloy. In the EBSD map (Figure 2b), low-angle boundaries (LABs) (misorientation < 15°) and high-angle boundaries (HABs) (misorientation > 15°) are shown with red and blue colors, respectively. Figure 2b also shows that the LABs which are known to show evidence of the sub-grain boundaries are mostly distributed within HABs. From Figure 2d, the fraction of HABs was measured to be approximately 60%. These results suggest that the alloy had experienced dynamic recrystallization during the extrusion process [10].
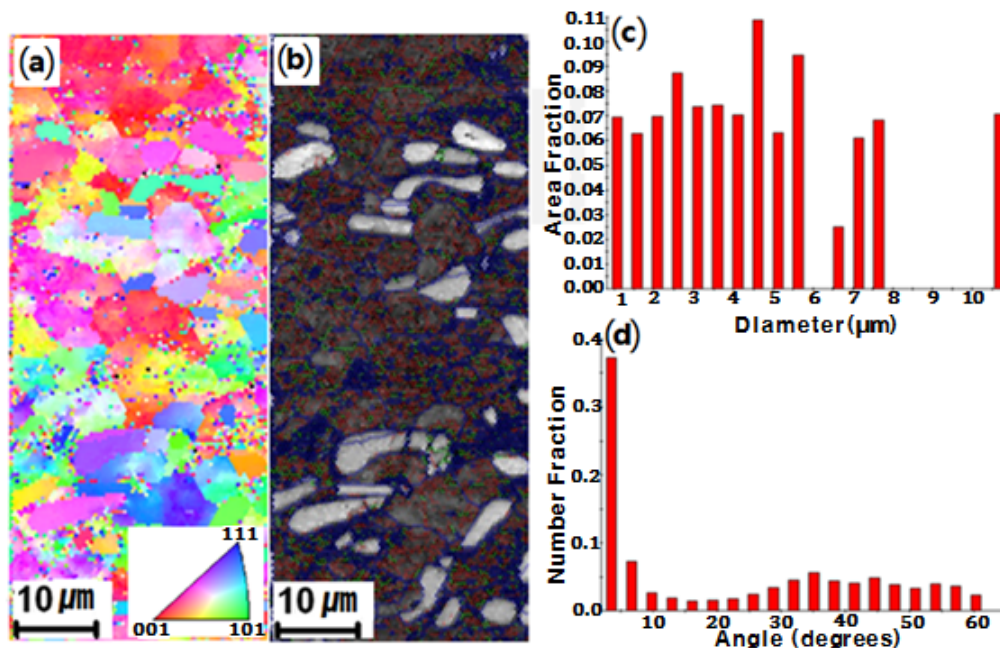

Figure 2. EBSD analysis data of the as-received alloy: (**a**) EBSD map (the insert in bottom right corner of (**a**) showing the representation of the color key used to identify the crystallographic orientations on a standard stereographic projection); (**b**) grain boundary misorientation map; (**c**) grain size distribution; (**d**) misorientation angle distribution.

3.2. Phase Analysis

　　　Figure 3 presents the JMatPro simulation data for the DM104 alloy, indicating the existing phases and their weight fraction during the solidification process. In the case of the equilibrium state (Figure 3a), eutectic Si and intermetallic T phase (Al_9FeNi) solidify at 560 °C and 550 °C, respectively. As the temperature decreased to less than 532 °C, the weight fraction of the T phase decreased with the formation of the δ(Al_3Ni_2 or Al_3NiCu) and Q($Al_8Cu_2Mg_8Si_6$) phases. The weight fraction of the δ phase decreased with increasing formation of the T and γ(Al_2Cu_4Ni) phase under 375 °C. At the end of the solidification process, the Si phase comprised approximately 11% of the weight fraction and every intermetallic phase comprised less than 5% of the weight fraction. Although the solidification temperatures of the main phases appeared to be similar among the results in Figure 3a,b, the weight fraction of each phase in the non-equilibrium state (Figure 3b) maintained a specific value until the end of solidification. Figure 3b shows that the δ, T and Q phases have considerable weight fractions.

　　　Figure 4 shows the XRD patterns of the as-received alloy, indicating the peaks of δ(Al_3Ni_2 or Al_3NiCu) and Q($Al_8Cu_2Mg_8Si_6$) phases in addition to the intensive peaks of Al and Si phases.

　　　Figure 5a shows a SEM image of the alloy. The phases labeled in Figure 5a were identified by EDS, and their chemical compositions are given in Figure 5b. The chemical compositions of points ② and ③ appear to correspond to the stoichiometric composition of the Q($Al_8Cu_2Mg_8Si_6$) and δ(Al_3NiCu)

phases, respectively. The δ and Q phases are frequently detected by SEM (Figure 5a), and these results are in accordance with both the XRD pattern in Figure 4 and the JMatPro simulation data in Figure 3.
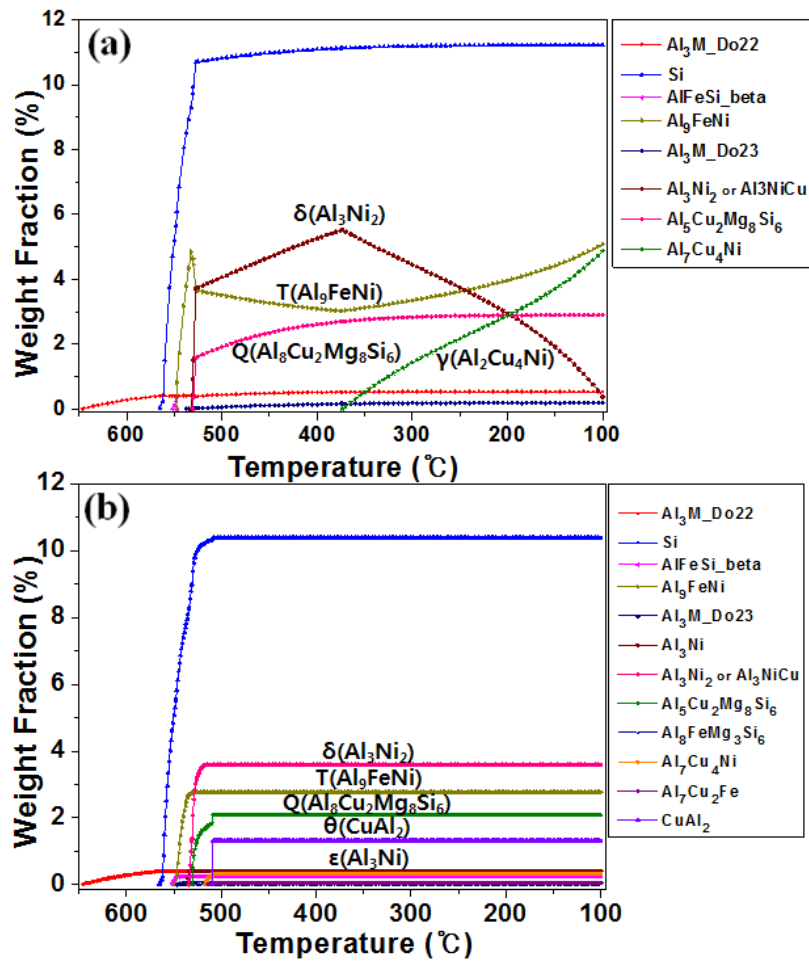

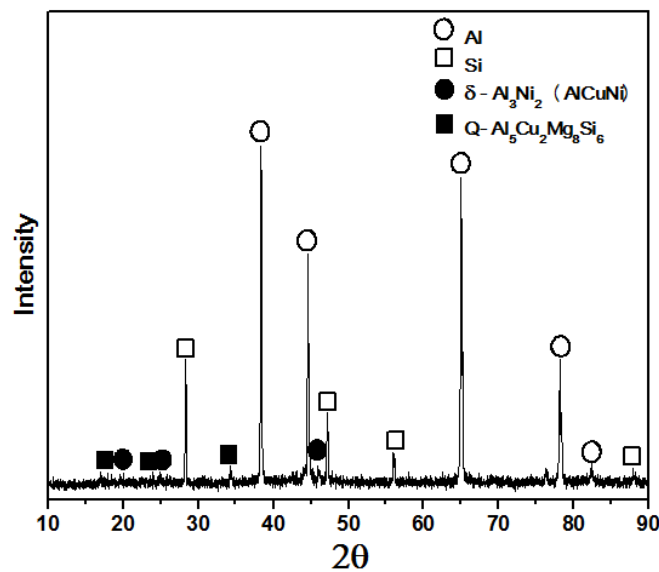**Figure 3.** JMatPro simulation data of the as-received alloy for (**a**) equilibrium; (**b**) non-equilibrium state.

Figure 4. XRD result of the as-received alloy.

(b) Element	Chemical composition (at%)				
	Point ①	Point ②	Stoichiometric Q Phase (Al₅Cu₂Mg₈Si₆)	Point ③	Stoichiometric δ Phase (Al₃CuNi)
Al	1.40	17.3	23.8	42.3	60
Si	94.0	30.4	28.6	2.15	–
Fe	3.07	3.24	–	3.55	–
Ni	0.58	0.85	–	26.3	20
Mg	0.14	28.0	38.1	1.52	–
Cu	0.81	20.2	9.5	21.2	20

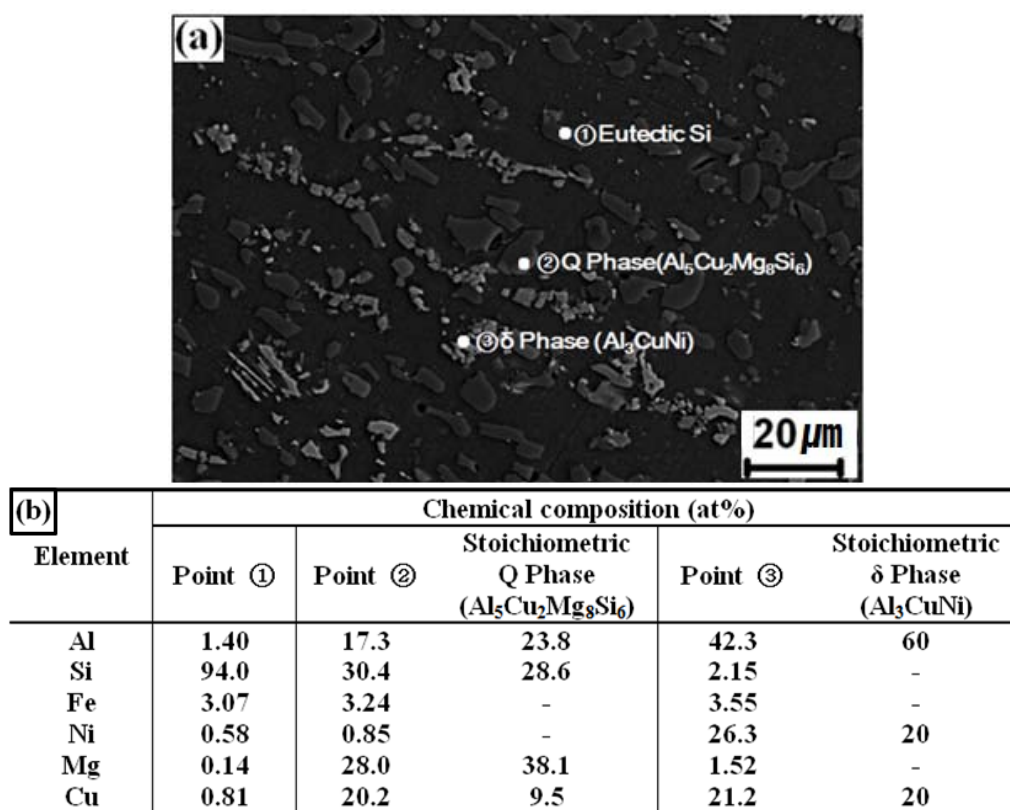**Figure 5.** (**a**) SEM image; (**b**) EDS analysis data of the as-received alloy.

3.3. Compressive Deformation

Figure 6 presents the true stress-true strain curves of the specimens compressive-tested at temperatures between 250 and 470 °C and strain rates between 0.001 and 1/s. The flow stress increased sharply with increasing strain at the initial stages of deformation. The flow stress then decreased and finally reached a steady-state with further increases in strain. The steady-state behavior was initiated at a lower strain range of deformation at a higher test temperature.
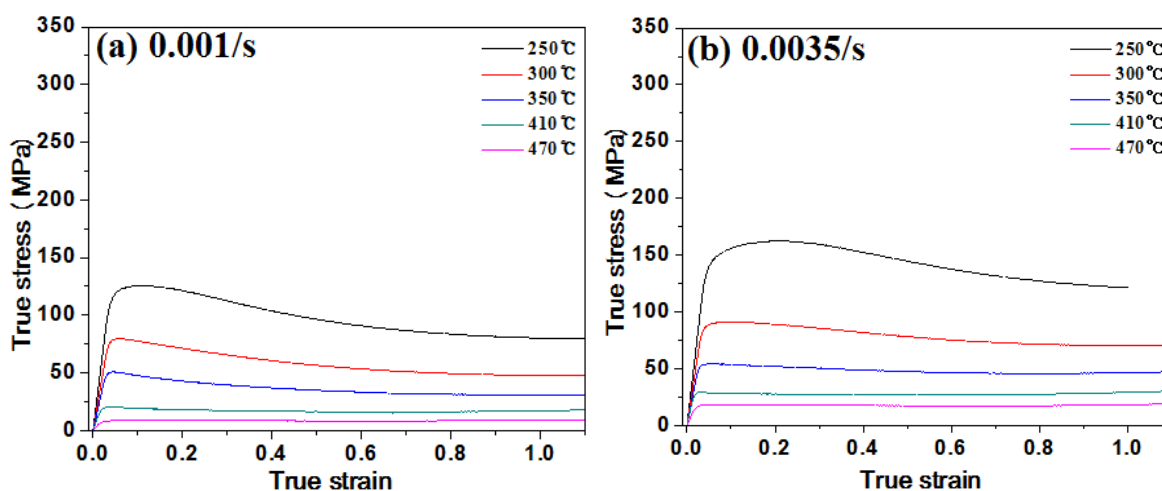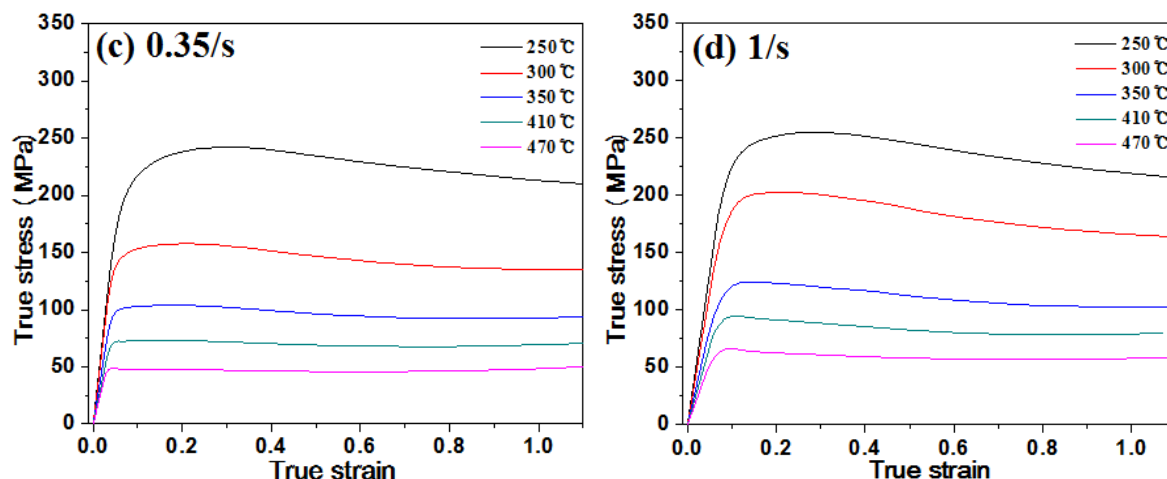

Figure 6. *Cont.*

Figure 6. True stress-true strain curves of the specimens compressed at various temperatures under a strain rate of (**a**) 0.001/s; (**b**) 0.0035/s; (**c**) 0.35/s; (**d**) 1/s.

Figure 7 shows the temperature-dependence of the steady-state stress for different strain rates. At a given temperature, the steady-state stress increased with increasing strain rate, and at a given strain rate, the steady-state stress decreased with increasing temperature.
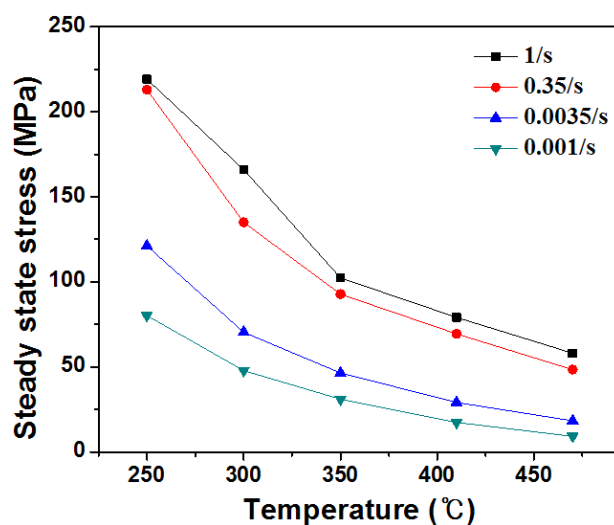

Figure 7. Variation of the steady-state stress with temperature at different strain rates.

3.4. Constitutive Equations

$$\acute{\varepsilon} = A_1 \sigma^n \exp(-\frac{Q}{RT}) : \text{ Power law} \tag{1}$$

$$\acute{\varepsilon} = A_2 \exp(\alpha\sigma) \exp(-\frac{Q}{RT}) : \text{ Exponential law} \tag{2}$$

$$\acute{\varepsilon} = A_3 [\sinh(\beta\sigma)]^{n'} \exp(-\frac{Q}{RT}) : \text{ Hyperbolic sine law} \tag{3}$$

Constitutive equations, such as Equations (1)–(3), have been used to describe the relationship between the stress (σ), temperature (T) and strain rate ($\dot{\varepsilon}$) during the high temperature deformation of an Al-based alloy [11–13]. A_1, A_2, A_3, n, n', α, and β ($=\alpha/n$) are material constants. In the present study, constitutive equations were deduced using the steady-state stress values from Figure 6. The power law,

Equation (1), and exponential law, Equation (2), break down at the higher and lower stress regions, respectively. In contrast, the hyperbolic sine law, Equation (3), is suitable for stresses over a wide range.

Figure 8a,b show linear plots of $\ln(\dot{\varepsilon})$-$\ln(\sigma)$ and $\ln(\dot{\varepsilon})$-σ for the deformed alloys, respectively. The average values of n and α were calculated from the slope in Figure 8a,b, respectively. The value of β ($\beta = \alpha/n$) was applied to the hyperbolic sine law, Equation (3). Figure 8c,d present linear plots of $\ln(\dot{\varepsilon})$-$\ln[\sinh(\alpha\sigma)]$ and $\ln[\sinh(\alpha\sigma)]$-1000/T for the deformed alloys, respectively. The mean values of n' and Q (activation energy) were calculated from the slope in Figure 8c,d, respectively. Table 2 presents the calculated constants from the above equations. As a result, the hyperbolic sine law of the alloy can be expressed as Equation (4).
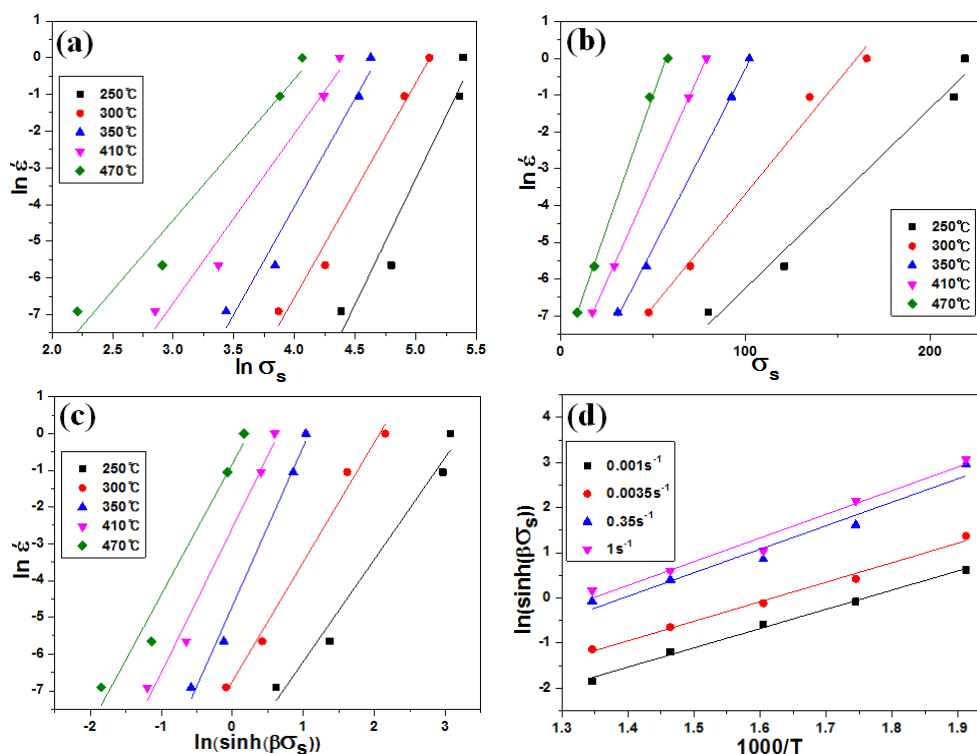

Figure 8. Relationship between steady-state stress, strain rate and temperature: (**a**) $\ln(\dot{\varepsilon})$ *versus* $\ln(\sigma)$; (**b**) $\ln(\dot{\varepsilon})$ *versus* σ; (**c**) $\ln(\dot{\varepsilon})$ *versus* $\ln[\sinh(\beta\sigma)]$; (**d**) $\ln[\sinh(\beta\sigma)]$ *versus* 1000/T.

$$\text{Hyperbolic sine law}: \dot{\varepsilon} = 5.3 \times 10^9 \left\{\sinh(0.017\sigma_s)\right\}^{3.57} \exp(-142000/RT) \tag{4}$$

Table 2. Material constants for the alloy, which were evaluated from the constitutive equations.

Constant	n	α	β	A_3 (s^{-1})	n'	Q (kJ/mol)
Value	5.41	0.093	0.017	5.3×10^9	3.57	142

3.5. Zener-Hollomon Parameter

The deformation temperature and strain rate are incorporated into the Zener-Hollomon (Z) parameter, Equation (5).

$$Z = \dot{\varepsilon}\exp(\frac{Q}{RT}) : \text{Zener-Hollomon } (Z) \text{ parameter} \tag{5}$$

$$Z = 5.3 \times 10^9 \left\{\sinh(0.017\sigma_s)\right\}^{3.57} \tag{6}$$

Equation (6), which gives the relationship between sinh($\beta\sigma$) and the Z parameter, can be obtained by combining Equation (4) with Equation (5).

The values of sinh($\beta\sigma$) calculated using Equation (6) are presented as a linear line in Figure 9. In this figure, the experimentally obtained sinh($\beta\sigma$) values are also included. As shown in Figure 9, the comparison between the experimental and calculated data revealed high similarity between the two datasets. Therefore, the constitutive equation, Equation (6), is reasonable for explaining the high temperature deformation behavior of the present alloy.
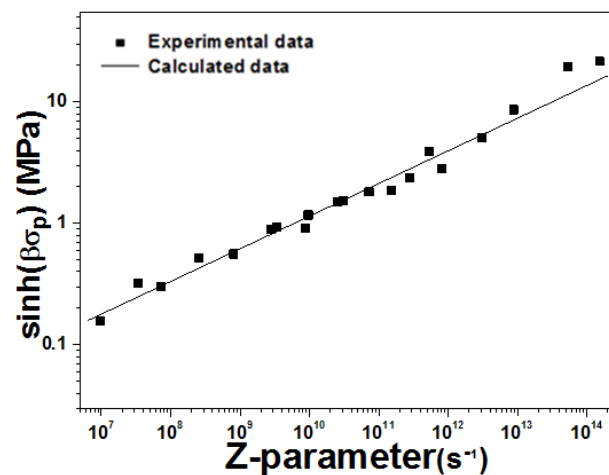

Figure 9. Comparison between the experimental and calculated data.

3.6. Microstructure of the Deformed Specimens

Figure 10 presents optical micrographs of the alloy deformed at a strain rate of 1/s and temperatures from 250 °C to 470 °C. Elongated grains were observed in the specimens deformed compressively at 250 °C (Figure 10a) and 300 °C (Figure 10b). In contrast, at 350 °C and above, equiaxed grains were visible near the eutectic Si particles and intermetallics, and the mean grain size of the equiaxed grains increased with increasing temperature. The large precipitates in Figure 10c–e were primary Si particles which may be generated by non-equilibrium solidification (hypereutectic solidification). Brittle primary Si particles were normally broken during the extrusion process, although some of them could remain after the extrusion.
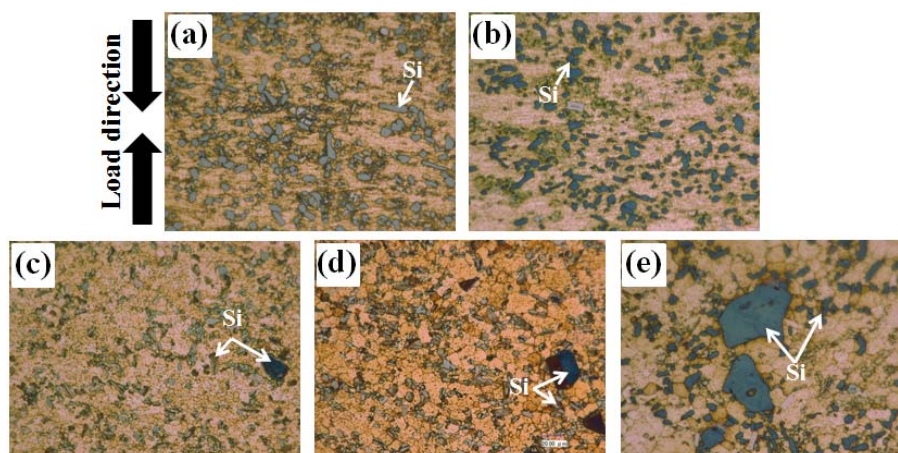

Figure 10. Optical micrographs of the deformed specimens at a strain rate of 1 /s at (**a**) 250 °C; (**b**) 300 °C; (**c**) 350 °C; (**d**) 410 °C; (**e**) 470 °C.

Table 3 lists the mean grain size after deformation under different test conditions. The mean grain sizes were in the range between 2.9 and 7.2 μm.

Table 3. Mean grain size (μm) after deformation under different test conditions.

Strain Rate (/s)	Temperature (°C)		
	350	410	470
1	2.9	3.2	4.1
0.35	3.3	3.4	4.5
0.0035	4.8	5.9	6.7
0.001	5.1	5.7	7.2

Figure 11a shows a TEM bright field image of the specimen deformed to 20% true-strain at 470 °C under a strain rate of 1/s. The 20% strain corresponds to a steady-state deformation region after reaching the peak stress (see Figure 6d). As shown in Figure 11a, fine dispersoids were distributed as indicated by points ② and ③. Figure 11b shows the EDS analysis data of points ② and ③, which appear to correspond to the stoichiometric composition of the δ(Al$_3$NiCu) phase. Figure 11a shows the dislocations within the equiaxed grains. The existence of both equiaxed grains and a dislocation structure within the equiaxed grains indicates that dynamic recrystallization occurred during the course of high temperature deformation of the present alloy.
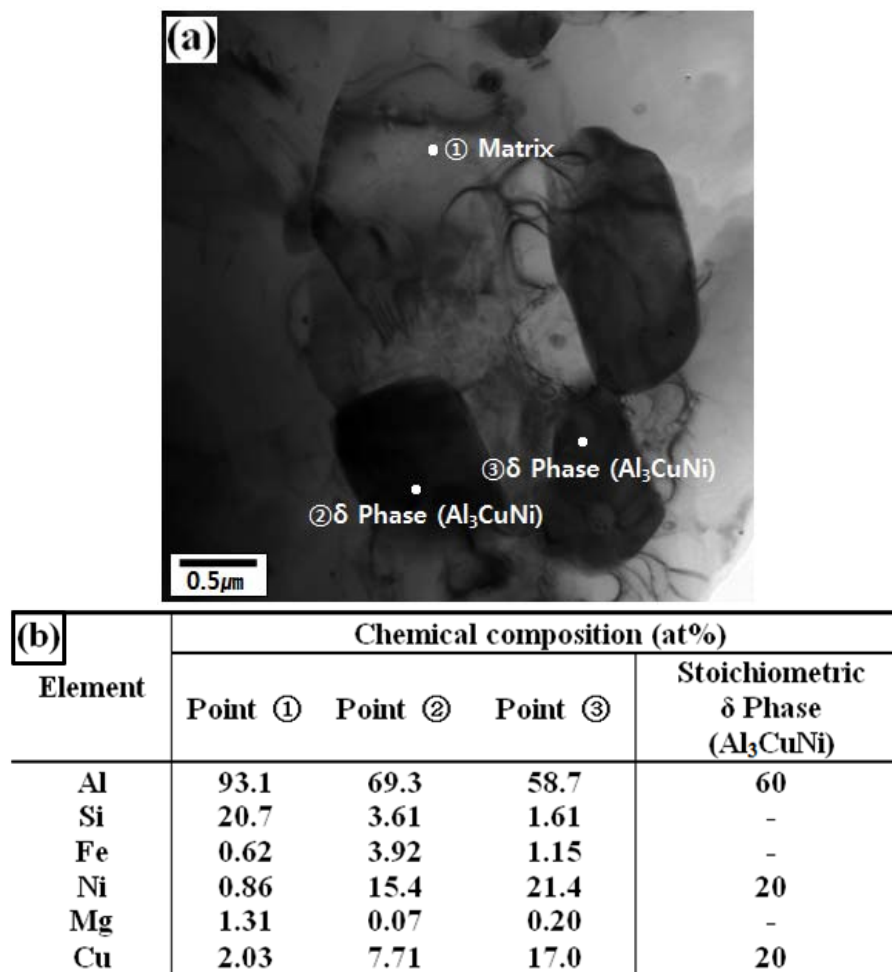

(b) Chemical composition (at%)

Element	Point ①	Point ②	Point ③	Stoichiometric δ Phase (Al$_3$CuNi)
Al	93.1	69.3	58.7	60
Si	20.7	3.61	1.61	-
Fe	0.62	3.92	1.15	-
Ni	0.86	15.4	21.4	20
Mg	1.31	0.07	0.20	-
Cu	2.03	7.71	17.0	20

Figure 11. (**a**) TEM image and (**b**) EDS data of the specimen deformed to 20% of true-strain at a strain rate of 1/s at 470 °C.

4. Conclusions

Compressive tests of the commercial Al-12Si-3Cu-2Ni-1Mg alloy (DM104™) fabricated by casting and subsequent extrusion were conducted over the temperature range, 250–470 °C, and strain rate range of 0.001–1/s. The following conclusions were obtained:

1. The as-received alloy had equiaxed grains with a mean grain size of approximately 5 μm, spherical Si particles and fine intermetallic phases including δ(Al_3NiCu) and Q($Al_5Cu_2Mg_3Si_6$).
2. EBSD analysis of the as-received alloy showed that the fraction of high-angle boundaries (HABs) was approximately 60%, and the low-angle boundaries (LABs) are distributed mostly as sub-grain boundaries within the HABs.
3. The true stress-true strain curves obtained from the compressive tests exhibited steady-state flow after reaching the peak stress.
4. The steady-state stress decreased with increasing temperature and decreasing strain rate. A close relationship was observed between the steady-state stress and a constitutive equation for high temperature deformation.
5. Fine equiaxed grains and a dislocation structure within the equiaxed grains were observed in the deformed specimens, indicating the occurrence of dynamic recrystallization during high temperature deformation.

Author Contributions: Study design: Mok-Soon Kim; Experimental work: Seung-Baek Yu; Results analysis & Manuscript preparation: All authors; Manuscript proof and Submission: All authors.

Conflicts of Interest: The authors declare no conflict of interest.

References

1. Manasijevic, S.; Radisa, R.; Markovic, S.; Acimovic-Pavlovic, Z.; Raic, K. Thermal analysis and microscopic characterization of the piston alloy AlSi13Cu4Ni2Mg. *Intermetallics* **2011**, *19*, 486–492. [CrossRef]
2. Chen, C.-L.; Thomson, R.C. The combined use of EBSD and EDX analyses for the identification of complex intermetallic phases in multicomponent Al-Si piston alloys. *J. Alloys Compd.* **2010**, *490*, 293–300. [CrossRef]
3. Kim, J.; Jang, G.S.; Kim, M.S.; Lee, J.K. Microstructure and compressive deformation of hypereutectic Al-Si-Fe based P/M alloys fabricated by spark plasma sintering. *Trans. Nonferrous Met. Soc. China* **2014**, *24*, 2346–2351. [CrossRef]
4. Park, S.-C.; Kim, M.-S.; Kim, K.-T.; Shin, S.-Y.; Lee, J.-K.; Ryu, K.-H. Compressive Deformation Behavior of Al-10Si-5Fe-1Zr Powder alloys Consolidated by Spark Plasma Sintering Precess. *Korean J. Met. Mater.* **2011**, *49*, 853–859.
5. Sjölander, E.; Seigeddine, S. The heat treatment of Al-Si-Cu-Mg casting alloys. *J. Mater. Processs. Technol.* **2010**, *210*, 1249–1259. [CrossRef]
6. Aguilera-luna, I.; Castro-Roman, M.J.; Escobedo-bocardo, J.C.; Garcia-Pastor, F.A.; Herrera-Trejo, M. Effect of cooling rate and Mg content on the Al-Si eutectic for Al-Si-Cu-Mg alloys. *Mater. Charact.* **2014**, *95*, 211–218. [CrossRef]
7. Zamani, M.; Seifeddine, S.; Jarfors, A.E.W. High temperature tensile deformation behavior and failure mechanisms of an Al-Si-Cu-Mg cast alloy—The microstrcutural scale effect. *Mater. Des.* **2015**, *86*, 361–370.
8. Cho, H.S.; Kim, M.S. High Temperature Deformation Behavior of Al-16Si-5Fe based alloys Produced from Rapidly Solidified Powders. *J. Korean Inst. Met. Mater.* **1999**, *37*, 1191–1197.
9. Li, Y.; Yang, Y.; Wu, Y.; Wang, L.; Liu, X. Quantitative comparison of three Ni-containing phases to the elevated-temperature properties of Al-Si piston alloys. *Mater. Sci. Eng. A* **2010**, *527*, 7132–7137. [CrossRef]
10. Wu, Y.; Liao, H.C.; Yang, J.; Zhou, K. Effect of Si content on Dynamic Recrystallization of Al-Si-Mg alloys During Hot Extrusion. *J. Mater. Sci. Technol.* **2014**, *30*, 1271–1277. [CrossRef]

11. Hu, H.E.; Wang, X.; Deng, L. High temperature deformation behavior and optimal hot processing parameters of Al-Si eutectic alloy. *Mater. Sci. Eng.* **2013**, *576*, 45–51. [CrossRef]

12. Zhang, H.; Li, L.; Yuan, D.; Peng, D. Hot deformation behavior of the new Al-Mg-Si-Cu aluminum alloy during compression at elevated temperatures. *Mater. Charact.* **2007**, *58*, 168–173. [CrossRef]

13. Liao, H.; Wu, Y.; Zhou, K.; Yang, J. Hot deformation behavior and processing map of Al-Si-Mg alloys containing different amount of silicon based on Gleebe-3500 hot compression simulation. *Mater. Des.* **2015**, *65*, 1091–1099. [CrossRef]